AUTHOR QUERY FORM

AIP Publishing	**Journal: Rev. Sci. Instrum.** **Article Number: 016805RSI**	**Please provide your responses and any corrections by annotating this PDF and uploading it according to the instructions provided in the proof notification email.**

Dear Author,

Below are the queries associated with your article. Please answer all of these queries before sending the proof back to AIP.

Article checklist: In order to ensure greater accuracy, please check the following and make all necessary corrections before returning your proof.
1. Is the title of your article accurate and spelled correctly?
2. Please check affiliations including spelling, completeness, and correct linking to authors.
3. Did you remember to include acknowledgment of funding, if required, and is it accurate?

Location in article	**Query/Remark: click on the Q link to navigate to the appropriate spot in the proof. There, insert your comments as a PDF annotation.**
Q1	Please check that the author names are in the proper order and spelled correctly. Also, please ensure that each author's given and surnames have been correctly identified (given names are highlighted in red and surnames appear in blue).
Q2	Please reword the sentence beginning with "Therefore, in order..." so that your meaning will be clear to the reader.
Q3	In sentence beginning "Thus, in Sec. V...," please confirm that "next section" refers to Sec. V.
Q4	We have merged the sentence beginning "In Ref. 51, in..." and "Since these hotter..." and reworded it for clarity. Please check that your meaning is preserved.
Q5	Please confirm the year of publication in Refs. 20, 45, and 46, as we have inserted the required information.
Q6	Please provide page number in Ref. 23.

Thank you for your assistance.

Analysis of wall-embedded Langmuir probe signals in different conditions on the tokamak à configuration variable

■Q1 O. Février,[1,a)] C. Theiler,[1] H. De Oliveira,[1] B. Labit,[1] N. Fedorczak,[2] and A. Baillod[1]
[1]*Swiss Plasma Center (SPC), École Polytechnique Fédérale de Lausanne (EPFL), CH-1015 Lausanne, Switzerland*
[2]*CEA, IRFM, F-13108 Saint Paul-lez-Durance, France*

(Received 15 January 2018; accepted 12 April 2018; published online XX XX XXXX)

This paper presents the current wall-embedded Langmuir probe system installed on the tokamak à configuration variable, as well as the analysis tool chain used to interpret the current-voltage characteristic obtained when the probes are operated in swept-bias conditions. The analysis is based on a four-parameter fit combined with a minimum temperature approach. In order to reduce the effect of plasma fluctuations and measurement noise, several current-voltage characteristics are usually averaged before proceeding to the fitting. The impact of this procedure on the results is investigated, as well as the possible role of finite resistances in the circuitry, which could lead to an overestimation of the temperature. We study the application of the procedure in a specific regime, the *plasma detachment*, where results from other diagnostics indicate that the electron temperature derived from the Langmuir probes might be overestimated. To address this issue, we explore other fitting models and, in particular, an extension of the asymmetric double probe fit, which features effects of sheath expansion. We show that these models yield lower temperatures (up to approximately 60%) than the standard analysis in detached conditions, particularly for a temperature peak observed near the plasma strike point, but a discrepancy with other measurements remains. We explore a possible explanation for this observation, the presence of a fast electron population, and assess how robust the different methods are in such conditions. https://doi.org/10.1063/1.5022459

I. INTRODUCTION

A surface in contact with a plasma acts as a sink for electrons and ions. Because of the higher mobility of the electrons, they will tend to reach the surface faster than the ions, resulting in the accumulation of negative charges on the surface, which will in turn repel electrons. This results in the formation of a *sheath*[1] close to the surface, a region where quasi-neutrality is not enforced.[2] If the surface potential is left floating, it will adjust itself so that the ion and electron currents reaching the surface counterbalance each other. However, if a voltage is imposed to the surface, then a current can flow. Measurements of this current can be used to derive essential properties of the plasma in the vicinity of the sheath. This idea is at the heart of the Langmuir Probe (LP),[3] a common diagnostic in plasma physics. By measuring the current reaching a probe to which a swept-bias potential is applied, it is possible to construct the so-called current-voltage characteristic (or I-V characteristic), which can then be used to derive plasma properties such as the electron temperature T_e, density n_e, and floating potential V_{fl}, by fitting a physical model to the data.[1,4] However, the interpretation of the measurements provided by the probes can be challenging, particularly for a magnetized plasma, as it occurs, for example, in a tokamak. The purpose of this paper is to present the standard analysis chain that is used to interpret the data obtained from the wall-embedded Langmuir probes on TCV[5,6] (*Tokamak à Configuration Variable*) at EPFL (*École Polytechnique Fédérale de Lausanne*) and to investigate alternative methods in non-standard situations and regimes where the default analysis is susceptible to misbehave. After briefly presenting the Langmuir probe system installed on the TCV tokamak (Sec. II), we detail the standard analysis workflow in Sec. III. After a first step consisting in the removal of possible stray currents from the measured signals, the I-V characteristics are fitted with a four-parameter model,[7–9] combined with a minimum temperature method.[10] We then investigate the impact of averaging several I-V curves before performing the fit, which allows reducing the effect of measurement noise and plasma fluctuations, assuming that the plasma is in stationary conditions. In non-stationary plasmas, for instance, in the H-mode with Edge Localized Modes (ELMs),[11] possible solutions to facilitate the fitting procedure are outlined. We furthermore provide an estimate of the error induced by the presence of resistance in the circuitry, which could yield an overestimation of the temperature. In Sec. IV, the standard analysis is applied to a discharge with varying conditions. We study a density ramp experiment, where the line-averaged density of the plasma is linearly increased during the discharge. In particular, we focus on a regime called *plasma detachment*,[12] where both density and temperature at the wall drop, and a pressure gradient develops along the magnetic field lines. We observe that the temperatures and densities derived from the Langmuir probe analysis tend to show the expected temperature and density drop, although the temperature can still attain between 5 and 10 eV in this regime across part of the wall,[13] while simulations and other measurements predict much lower temperatures. In particular, we observe a strong temperature peak in a certain part of the profile that

a)olivier.fevrier@epfl.ch

seems to be in contradiction with the expected physics. This could be an indication of a possible shortcoming of the analysis procedure. In addition, we observe a significant change of the I-V curve shape around detachment, with a reduction of the ratio between the electron and ion saturation currents. Therefore, to further investigate these issues, we explore other fitting models that can be used instead of the four-parameter fit in detached conditions. We first take advantage of the expected relation between the plasma potential and the floating potential to obtain another estimate of the temperature. We also introduce the Asymmetric Double Probe (ADP) model with sheath expansion, which folds in information from the entire I-V characteristic (Sec. V) and which could, in principle, yield more reliable results in detached conditions. These alternative fitting methods are included in the analysis chain as auxiliary estimates of the electron temperature. We show that in attached conditions, all the three methods are in relatively good agreement and agree relatively well in detached conditions far from the strike point. Near the strike-point, however, the two alternative methods do not show the strong temperature peaking observed with the four-parameter fit, an indication that it is indeed due to misbehavior of the four-parameter fit technique. Finally, in Sec. VI, we investigate the possible effect of a fast electron population on the inferred electron temperature, as their presence in detached plasma is strongly suspected.[14]

II. THE TCV LANGMUIR PROBE SYSTEM

The TCV wall-embedded Langmuir probe system[15] is currently composed of 114 Langmuir probes (LPs). The cylindrical probe tips are made of graphite and have a 4 mm diameter. The probes are embedded flush into the tiles except for a few rooftop probes and the floor probes, which have a dome-shaped head, protruding from the tile shadow by 1 mm. Figure 1 shows a picture of the three different probe heads installed in TCV. The locations of the probes are shown in Fig. 2, where a color code is used to distinguish the different kind of probes.

Data are acquired at 200 kHz, and for each probe, two operational modes are possible:

1. No biasing is applied to the probe, which is therefore left floating. It accumulates charges such that the collected current is zero, and the associated potential, the so-called floating potential, is measured.

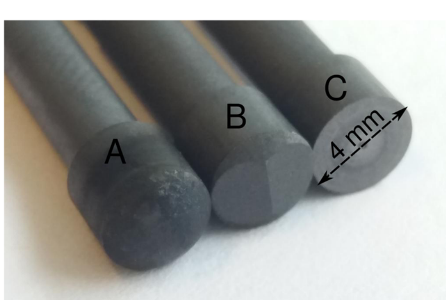

FIG. 1. Picture of the different probe heads installed in TCV. A: dome-shaped head. B: rooftop. C: flush.

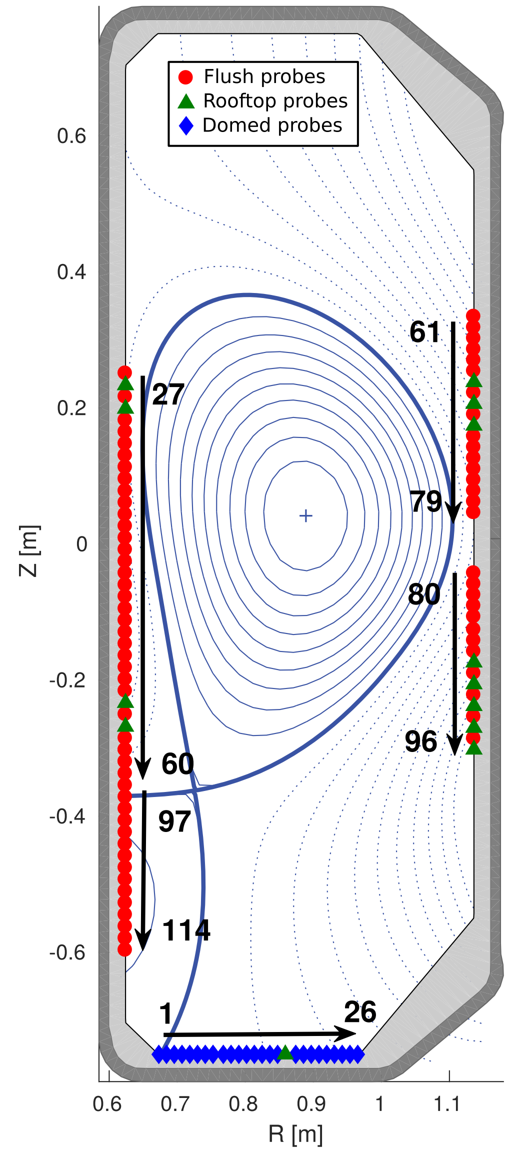

FIG. 2. Positions of the currently installed Langmuir probes in the TCV vacuum vessel walls. For illustration purpose, a typical plasma geometry is plotted (shot #52062). The different colors and symbols indicate the type of the probe. Red circle: flush embedded. Green triangle: rooftop. Blue diamond: dome.

2. An arbitrary biasing voltage in the range ±120 V relative to the machine ground is applied to the probes, and the current collected by the probe is measured.

In this article, we focus on the second operational mode and, in particular, on swept-bias, where the voltage V_{pr} applied to the probes is a triangular signal of given frequency (typically 330 Hz) and amplitude (typically ranging from −100 V to 80 V), thus allowing us to construct I-V characteristics of the plasma response in the vicinity of a probe, as illustrated in Fig. 3.

III. STANDARD ANALYSIS

This section describes the standard analysis chain implemented at TCV to analyze the measurements from the Langmuir probe system.

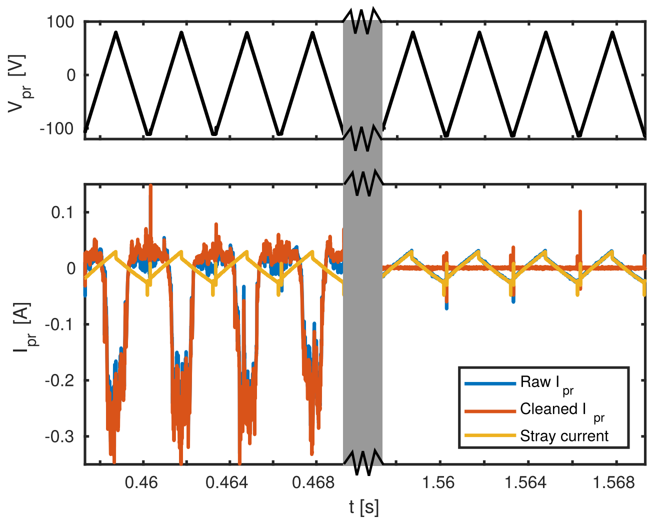

FIG. 3. (Top) Voltage sweep applied to an LP. (Bottom) Associated current collected by the probe (blue curve). The yellow curve shows the stray current caused by the circuitry, and the red curve shows the "cleaned" current resulting from the subtraction of the stray current from the measured current.

A. Removal of stray currents

Because of the non-ideality of the circuitry, the presence of stray currents in the system cannot be excluded. In order to evaluate them, voltage sweeps are acquired after the termination of the plasma, when the currents provided by the probes should be $I_{pr} = 0$. Therefore, the only currents that are measured are the stray currents I_{stray} coming from the circuitry. I_{stray} can then be reconstructed by averaging the measured patterns over a few sweep cycles (typically 50) to provide $I_{stray}(V_{pr})$, and, assuming that the stray currents do not change during a discharge, it is then possible to subtract them from the measured signals, thus giving a "clean" I_{pr}. Such a process is illustrated in Fig. 3, which shows the current measured by an LP operated with a swept voltage (shown in the top panel of Fig. 3). The measured current is plotted in blue in the bottom panel of Fig. 3. For each probe, a few sweeps performed after the termination of the plasma are used to determine the stray current I_{stray}, plotted in yellow in Fig. 3. I_{stray} is then removed from the measured current to reconstruct the "cleaned" current I_{pr}, plotted in red in Fig. 3. By subtracting I_{stray} from the collected current, one ensures that the current to be analyzed only stems from the plasma and not the circuitry. In Fig. 4, we have plotted the effect of the stray current removal on the obtained I-V characteristics for this specific case. We observe that, in the absence of stray current removal, there is a difference between upward and downward sweeps in the ion saturation branch of the I-V curve. In particular, downward sweeps (and, to a lesser extent, upward sweeps) show an unphysical drop of the measured current at low V_{pr}. This is however not seen on the "clean" current I-V characteristic, obtained by removing the stray current. The stray current removal is performed routinely and automatically at the beginning of the Langmuir probe analysis chain.

B. Fitting model

The standard interpretation of the I-V characteristic in TCV is performed using a four-parameter model[7,9] that links

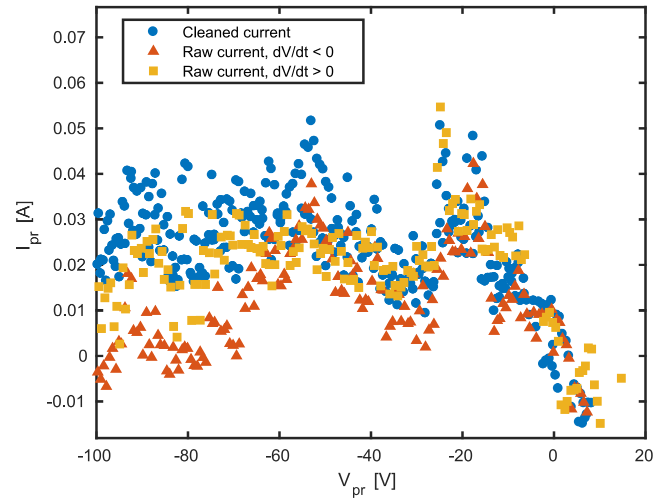

FIG. 4. Example of an I-V curve reconstructed during a complete voltage sweep (one voltage up and one voltage down phase) with and without the removal of stray currents, for the probe considered in Fig. 3. For readability of the figure, we zoomed in on the ion saturation part of the curve.

the measured current I_{pr} to the voltage V_{pr} applied to the probe, as follows:

$$I_{pr} = I_{sat}\left(1 + \alpha\left(V_{pr} - V_{fl}\right) - e^{\frac{V_{pr}-V_{fl}}{T_e}}\right). \tag{1}$$

Here, V_{fl} is the floating potential, that is, the potential at which the probe draws no current from the plasma. α accounts for the effect of sheath expansion.[16] T_e (expressed in eV) is the electron temperature, and I_{sat} corresponds to the ion saturation current. The saturation current is linked to n_e and T_e via the Bohm condition,[1,4]

$$I_{sat} = n_{e,se} e c_s S, \tag{2}$$

where $n_{e,se}$ is the electron density at the entrance of the sheath and $c_s = \sqrt{\frac{\gamma T_i + T_e}{m_i}}$ is the ion sound speed, with γ being the adiabatic index. In the following, we use $\gamma = 1$ and $T_i = T_e$, unless stated otherwise. It should be noted that when $\gamma = 1$, c_s corresponds to the sound speed of an isothermal plasma. In non-isothermal situations, depending on the assumptions made on the collisionality, the value of γ should be comprised between $5/3$ and 3 (see Refs. 1, 2, and 17). In Ref. 18, the value $\gamma = 3$ is used. In our case, we use $\gamma = 1$ as a default value to assure backward compatibility with previous TCV studies which assumed this value. It is however an input parameter of the analysis that can be changed if necessary. S is the effective ion collection area of the probe and is taken as the projected area of the probe along the magnetic field, with the latter determined from the equilibrium reconstruction code LIUQE[19] and typically forming an angle with respect to the wall of about 0° to about 10°. Equation (2) thus allows evaluating the electron density $n_{e,se}$ near the wall from the value of I_{sat} and T_e determined from the fit. In order to better model the current collected by the probe, the sheath expansion effect[16] is added. It corresponds to the modification of the sheath thickness due to the presence of the biased probe. While analytical expressions have been developed to model this phenomenon in the case of flush-mounted[18,20,21] and cylindrical probes,[22] we opted for a simpler formulation based on a linear reduction of the ion current as the probe voltage is increased,[7] the rate of the modification being set by the additional fit parameter α, defined such that $\alpha < 0$.

A difficulty in the I-V curve fitting procedure is that Eq. (1) is only valid at most up to the plasma potential V_{pl} and thus is not able to model the electron current saturation. In practice, the I-V curve already deviates from the exponential decrease well below V_{pl}. Therefore, in order to fit I-V characteristics, a supplementary step is added so as to find an upper limit of V_{pr} over which to apply Eq. (1). In the standard analysis procedure, we use the *minimum temperature* method.[10] At first, a non-physical fit of the data is done using a modified hyperbolic tangent function, presented in Appendix B, allowing us to invert the I-V characteristic to obtain $V_{pr} = V_{pr}(I_{pr})$. A discrete grid $\{r_n\}_{n=1,\ldots,N}$, where $r_n \in \mathbb{R}_+$, is specified by the user and used to determine a discrete set of cut-off voltages $\{V_n^*\}_{n=1,\ldots,N}$ defined by $V_n^* = V_{pr}(-r_n I_{sat}^{est})$, where I_{sat}^{est} is an estimate of I_{sat} based on the first (lowest voltage) points of the characteristic. The I-V curve is then fitted on each interval $\left[\min(V_{pr}), V_n^*\right]_{n=1,\ldots,N}$. Among the N individual fits obtained in this way, the one which returns the lowest temperature is then retained.

The minimum T_e approach avoids that a too large fraction of the curve is fitted, which would result in an overestimation of T_e. The choice of the grid $\{r_n\}_{n=1,\ldots,N}$ used to apply the minimum temperature method is however critical. For individual I-V curve fitting, if the chosen grid is too fine, then the algorithm can pick up on noise or fluctuations occurring on a faster time scale than the sweeping period (which is typically the case for plasma edge turbulence) and will return temperatures much lower than realistic. Such a case is illustrated in the top panel of Fig. 5, where we have plotted the current collected by an LP and the associated naive *minimum temperature* fit. One can see that in this situation, the minimum temperature approach leads to a low cut-off value for the fit ($V_{cut} \approx 1.9$ V), and a large part of the characteristic has been discarded. The fit appears to have picked up on fluctuations. A possibility to avoid this problem is to choose a coarser grid and check that the fit did not pick up on fluctuations. A better solution often consists in aggregating several I-V characteristics over a given time-window (typically 50 ms in our analysis) in order to get more points and thus reduce the effect of fluctuations.[18] To further enhance the stability of the minimum temperature method, the I-V data are also binned to produce an averaged I-V characteristic that is reasonably smooth. This is plotted in the bottom panel of Fig. 5, where the data points correspond to the data acquired for a period of 50 ms, corresponding to $\approx$32 voltage sweep cycles. The cut-off threshold determined by the procedure is higher ($V_{cut} \approx 6.5$ V) than that in the case of the single I-V fitting case, and a larger part of the (binned) I-V characteristic has been fitted, which ultimately leads to a derived temperature that is higher than that in the previous case. In both cases, we used $\{r_n\} = \left\{(n-1)\frac{6}{39}\right\}_{n=1,\ldots,40}$. This grid has been chosen based on the observation of the general aspect of the I-V curves in TCV and generally yields satisfactory results when fitting aggregated I-V curves.

We now focus on the effect of aggregating data from multiple I-V characteristics and then binning the data, when

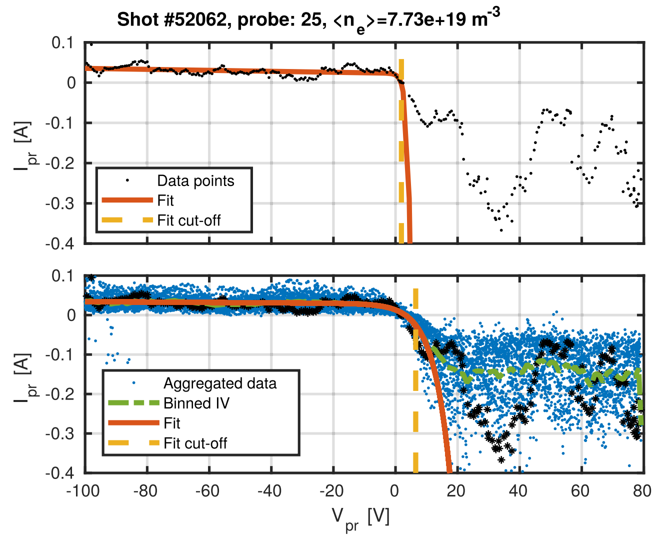

FIG. 5. (Top) Four-parameter fit associated with the minimum temperature method of a single I-V characteristic that features a high level of fluctuations. The points represent the measurements, while the red curve corresponds to the fit that has been determined by the method. The vertical line indicates the voltage cutoff that has been determined by the minimum temperature approach. (Bottom) Typical aggregated I-V data (blue dots) and binned I-V curve (green dashed curve). The red curve is the fit of the averaged I-V curve using the 4 parameter model described by Eq. (1). The data points from the single I-V curve in the top plot are highlighted by black stars. $\langle n_e \rangle$ refers to the line-averaged density of the plasma.

compared to a fit of each characteristic with a good choice of the voltage grid $\{r_n\}_{n=1,\ldots,N}$. In Fig. 6, two temperature profiles are plotted as a function of the radial coordinate ρ_ψ, which is the normalized poloidal magnetic flux, defined as $\rho_\psi = \sqrt{(\psi - \psi_0)\,/\,(\psi_1 - \psi_0)}$, where ψ is the poloidal magnetic flux and ψ_0 and ψ_1 are its value at the magnetic axis and at the primary X-point, respectively. The blue profile in Fig. 6 has been obtained after fitting the average of I-V

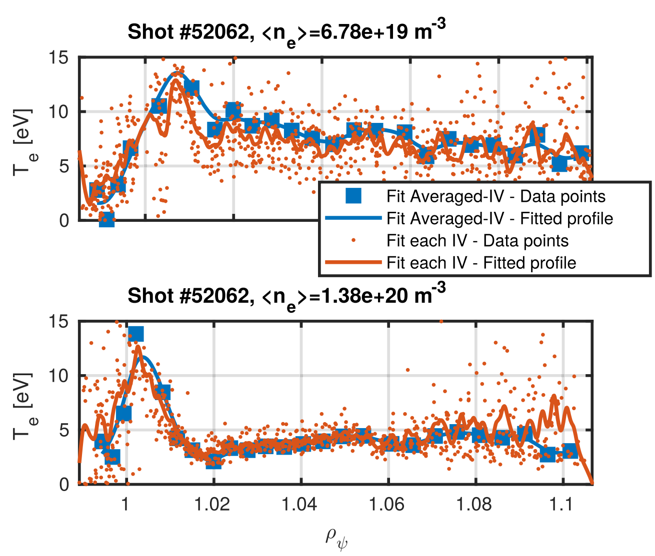

FIG. 6. Profiles of T_e showing the impact of I-V characteristics averaging before the fitting procedure, compared to averaging the data points after fitting. (Top) High temperature (>5 eV) case. (Bottom) Low temperature (<5 eV over most of the profile) case.

curves on a 50 ms time span, using $\{r_n\} = \left\{(n-1)\frac{6}{39}\right\}_{n=1,\ldots,40}$. The red data points have been obtained by fitting independently each I-V curve from the 50 ms time span, and the red profile represents the interpolation of this data. To limit the pickup on fluctuations in this case, we use a coarser grid, defined by using $\{r_n\} = \{1, 2, 3, 4, 6, 8\}$. The profiles resulting from the two methods are similar, even if one observes, as expected, a larger scatter of the data points when each I-V curve is fitted separately. Therefore, in cases with stationary turbulence that do not feature fast mesoscale fluctuations such as ELMs or fast strike-point sweeping, averaging the I-V curves before fitting yields very satisfactory results while being simple to use. A similar conclusion was obtained on the TORPEX device,[23] where fitting-aggregated I-V curves provided profiles very similar to those obtained from time-averaging measurements from a triple probe.[9] This technique is therefore the default strategy that is used in the analysis tool chain.

Averaging and binning I-V data are however not well adapted to non-stationary conditions, for instance, in cases of fast strike-point sweeping or during the H-mode, where ELMs can occur during a sweep. In the former case, reducing the time-window used for aggregating the data or applying the minimum temperature method to single I-V characteristics can be used to retrieve the averaged profiles. In the latter case, beyond these two previous methods, one can also consider excluding a subset of "contaminated" data points before performing the averaging, thus allowing us to obtain the inter-ELM profiles. Figure 6 illustrates that performing a single I-V curve fitting is possible. This generally requires the user to test several values and assess visually the goodness of the fits. A dedicated GUI has been developed to allow the user to plot both experimental data points and fits, so as to ensure the robustness of the latter.

In our analysis chain, the experimental data are fitted to the model described in Eq. (1) using a non-linear least square approach based on the Levenberg-Marquardt algorithm. Matlab is used to retrieve and prepare the data for the analysis, while the fitting in itself is done by a Fortran routine relying on the MINPACK library.[24,25] This allows a speed-up of more than an order of magnitude with respect to the previous analysis, which was written entirely in Matlab. The complete analysis chain, using a typical set of parameters, can be done in less than 10 min. Results are written to the MDSplus[26] tree and can be inspected with a Matlab GUI, thus allowing for inter-shot analysis.

C. Possible impact of resistance

In the case of the presence of resistances in the circuitry, the voltage actually applied to the probe is different than the voltage set by the voltage source. If we denote with R the possible resistance in the circuitry and V_{ms} the applied voltage, the actual probe voltage is given by

$$V_{pr} = V_{ms} + RI_{pr}. \tag{3}$$

Thus, a finite R will affect the shape of the I-V curve and lead to its expansion around the floating potential. This might lead to an over-estimation of the temperature and more generally to an incorrect determination of the different parameters. In TCV, considering the circuit going from the probe to the amplifier, an overall resistance can be estimated. Along the circuit, there are at least 4 electrical contacts of unknown resistance. We will assume for them a resistance of ∼0.1 Ω per contact. There is also 2.5 m of thermocoax cable, with a line resistance of 0.23 Ω/m, and 15 m of cable follows with a line resistance of 0.0336 Ω/m. The estimated overall resistance is therefore around 1.5 Ω. Note that the goal of this section is merely to evaluate how much the presence of resistance in the circuit can affect the measurements and not to give an absolute and precise quantification of this effect in our measurements. By inserting Eq. (3) into Eq. (1), and assuming $\alpha = 0$, we obtain

$$I_{pr} = I_{sat}\left(1 - e^{\frac{V_{ms}+RI_{pr}-V_{fl}}{T_e}}\right). \tag{4}$$

Equation (4) can be recasted in the form $ae^x + bx + c = 0$, and thus, following Appendix A, the expression for the current reaching the probe becomes

$$I_{pr} = I_{sat} - \frac{T_e}{R} W_0\left(\frac{RI_{sat}}{T_e} \mathrm{e}^{\frac{V_{ms}-V_{fl}+RI_{sat}}{T_e}}\right), \tag{5}$$

where W_0 is the 0-th branch of the Lambert W function.[27,28] It should be noted that for the sake of simplicity, we did not include the effect of sheath expansion in Eqs. (4) and (5), but it is straightforward to do so. One can check that for $V_{ms} = V_{fl}$, Eq. (5) yields $I_{pr} = 0$. Therefore, R does not affect the floating potential measurement. From Eq. (5), one can estimate what is the impact of the resistance R on the derived temperature. Starting from Eq. (1) and assuming no resistance ($R = 0$, leading to $V_{ms} = V_{pr}$), the temperature T_e can be estimated as

$$\frac{1}{T_e} = -\frac{1}{I_{sat}} \left.\frac{\mathrm{d}I_{pr}}{\mathrm{d}V_{ms}}\right|_{V_{ms}=V_{fl}}. \tag{6}$$

Denoting T_e^{eff} as the temperature that would be estimated from Eq. (6) applied to Eq. (5), we have

$$\frac{1}{T_e^{eff}} = -\frac{1}{I_{sat}} \left.\frac{\mathrm{d}I_{pr}}{\mathrm{d}V_{ms}}\right|_{V_{ms}=V_{fl}} = \frac{1}{T_e} \frac{1}{1+\frac{I_{sat}R}{T_e}}, \tag{7}$$

and therefore

$$T_e^{eff} = T_e\left(1 + \frac{I_{sat}R}{T_e}\right). \tag{8}$$

Using Eq. (2), this analysis shows that the determined temperature is overestimated by a factor scaling as

$$\Delta T_e^{th} = \frac{I_{sat}R}{T_e} \propto \frac{Rn_e}{\sqrt{T_e}}. \tag{9}$$

Therefore, we expect to see a manifestation of this effect for high density and low temperature plasmas. It should be noted that the scaling of the temperature error we determined is based on using the derivative of the I-V characteristic at $V_{ms} = V_{fl}$. However, in the standard analysis chain, the temperature that we derive is instead determined by fitting globally the characteristic to Eq. (1). Thus the error in the determination of T_e could differ from the evaluation done in Eq. (9). To evaluate this, we generate a set of synthetic curves using Eq. (1). We choose $R = 1.5$ Ω, $V_{fl} = 5$ V, $\alpha = 0$, and $S = 3.0 \times 10^{-6}$ m^2, and we vary n_e and T_e. I_{sat} is evaluated from Eq. (2). Once

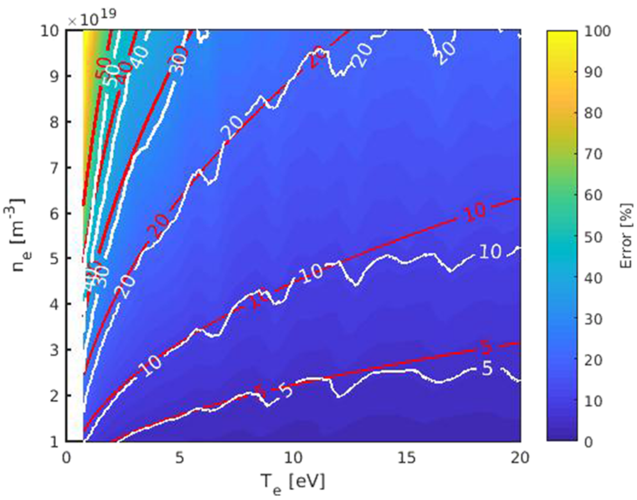

FIG. 7. Evolution of ΔT_e^{fit} (expressed in %) as a function of n_e and T_e for a stray resistance of 1.5 Ω and $S = 3.0 \times 10^{-6}$ m^2. The white lines are iso-contours of ΔT_e^{fit}. The red lines correspond to the scaling predicted by Eq. (9).

the curve $I_{pr} = I_{pr}(V_{pr})$ has been generated, we substitute the voltage values to reflect the existence of resistance in the circuit, $V_{pr} \leftarrow V_{pr} - RI_{pr}$. Note that this is equivalent to using directly Eq. (5) since it is just a change of variables. The curves are then fitted using the four-parameter fit, and we evaluate the error ΔT_e defined as

$$\Delta T_e^{fit} = \frac{T_e^{fit} - T_e}{T_e}, \tag{10}$$

where T_e^{fit} is the temperature determined by a four-parameter fit with minimum temperature and T_e is the temperature used to construct the synthetic I-V. In Fig. 7, we have plotted the variation of ΔT_e^{fit} as a function of n_e and T_e. While for low densities the effect appears to be negligible, it starts to play a more significant role at higher n_e, where I_{pr} tends to be larger and can therefore more strongly modify the voltage at the probe. It also appears that the effect of the resistance is slightly more pronounced in the low-T_e domain. This is in line with the conclusions drawn previously, as shown by the red lines, which corresponds to the iso-contours obtained from Eq. (9) and which are similar to the iso-contours of ΔT_e^{fit}, indicating that Eq. (9) gives a consistent scaling of the error with n_e and T_e.

IV. APPLICATION TO DETACHED PLASMAS

Large temperature gradients can develop along the magnetic flux tubes linking the upstream *Scrape-Off Layer* (SOL, the region of open field lines outside the separatrix of the plasma) to the wall. Depending on the local temperature, different volumetric processes can occur. For instance, for temperatures in the range from about 10 eV to a few tens of eV, low-Z impurities are susceptible to radiate power isotropically, thus distributing the exhaust power over a larger area and therefore reducing the peak heat fluxes reaching the divertor wall. If the temperature further drops (below approximately 5 eV), charge exchange reactions between plasma ions and neutrals can result in a net loss of momentum and energy from the plasma. This yields a drop of the pressure along the magnetic field lines and is usually denoted as *detachment*.[12,29] This process is enhanced below ∼1.5 eV, when volume recombination can become an important particle sink. Since in these conditions the temperature and density at the wall are reduced, detached regimes appear as an attractive solution for future fusion devices, as they could effectively protect the wall from enormous local peak heat fluxes and unacceptable sputtering rates. In this section, we investigate the possibility to use the Langmuir probes to measure the temperature at the wall in detached conditions, which is generally considered to be a difficult regime for Langmuir probe measurement interpretation.[30–32] Indeed, it has been seen in several tokamaks,[33,34] including TCV,[31,32] that in detached conditions, the Langmuir probe analysis yields electron temperature higher than that one would expect from other diagnostics such as spectroscopy,[35–37] Thomson scattering,[29,38] or simulations.[31] Several mechanisms might be responsible for this effect, such as the role of plasma resistance[1,39] or the fluctuations of the floating potential.[39] Furthermore, the standard fitting procedure considers only a relatively small part of the I-V characteristics, the one determined by the high energetic electrons of the distribution.[40] In the case of a significant departure of the electron distribution from a Maxwellian, the Langmuir probes then measure mostly the temperature of the hot electron population. Such a departure from the Maxwellian distribution has been observed in simulations[14,41] and experiments[42] and could explain the overestimation of the temperature.

In Fig. 8, the electron temperature and density radial profiles on the floor wall are plotted for an experiment where

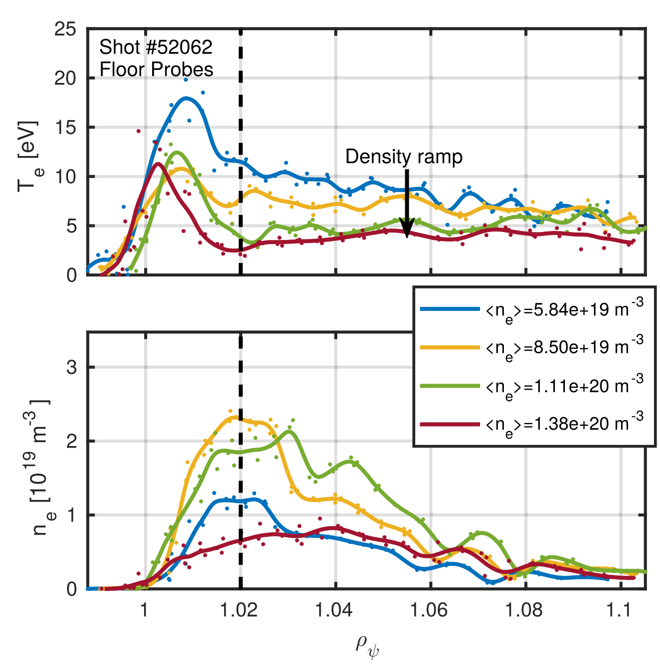

FIG. 8. Temperature (top) and density (bottom) profiles measured by the floor probes at different times in a density ramp experiment in TCV, where the line-averaged density of the plasma is linearly increased during the discharge. As line-averaged density is increased, the temperature measured at the wall decreases. After an initial growth, the density measured at the wall also decreases after detachment. The four-parameter fit with the minimum temperature approach is used to determine T_e and n_e at the wall. The dashed line at $\rho_\psi = 1.02$ indicates the mean position (over time) of the density profile peak.

plasma line-averaged density $\langle n_e \rangle$ is increased approximately linearly over time. The magnetic configuration is the same as in Fig. 2. In the top panel, a clear decreasing trend can be seen on the temperature profile as the line-averaged density is increased. This is a possible indication of detachment, which is further confirmed when measuring the total ion flux reaching the wall, which decreases above a certain line-averaged density, as shown in Ref. 13 or, for a single probe, in the top panel of Fig. 11. In the bottom panel of Fig. 8, the evolution of the density profile is also plotted. After an initial rise, the measured density finally decreases after detachment. In a similar discharge, measurements with divertor spectroscopy (based on collision-radiation model, without transport) found significant levels of volume recombination at the highest $\langle n_e \rangle$, suggesting $T_e \leq 1$ eV (Ref. 43).

A striking feature of the profiles plotted in Fig. 8 is the existence of a temperature peak near the strike-point position (i.e., the point where the separatrix intersects the wall, at $\rho_\psi = 1$), on the left ("high-field side") of the density profile. Even at $\langle n_e \rangle \approx 1.38 \times 10^{20}$ m^{-3}, the electron temperature reaches values of the order of 10 eV, while the plasma is expected to be detached. The presence of this peak is not yet fully understood. Observations on a restricted dataset indicate that the peak occurs in the region of positive radial density gradient and is more visible at higher flux expansion, which also corresponds to the cases where the ion flux to the wall is reduced the most, an indication of stronger detachment.[13]

One might suspect that this peak is unphysical and comes from a difficulty of the four-parameter fit to operate for certain shapes of I-V curves. We show in the following that the sheath physics offers another way to estimate the electron temperature and that, in the region of the temperature peak, the discrepancy between these two evaluations of the temperature might indeed indicate a failure of the four-parameter fit technique. When the probe is biased at a potential higher than the plasma potential V_{pl}, it is no longer repulsing the electrons, and the current collected by the probe saturates. It is possible to show that the difference between the plasma potential V_{pl} and the floating potential V_{fl} can be written, when including the voltage drops in the sheath and pre-sheath, as[1]

$$V_{pl} - V_{fl} = \Lambda T_e, \tag{11}$$

where

$$\Lambda = \ln\left(\sqrt{\frac{2m_i}{\pi m_e}\left[\frac{T_e}{T_e + \gamma T_i}\right]}\right). \tag{12}$$

For a typical deuterium plasma, assuming $\gamma = 1$ and $T_i = T_e$, which are the default assumptions made in our analysis, one finds $\Lambda \approx 3.53$. Under the assumption that the voltage at which the current collected by the probe saturates does correspond to the plasma potential V_{pl}, and by measuring the floating potential of the probe, it is possible to infer the electron temperature as

$$T_e = \frac{\left(V_{pl} - V_{fl}\right)}{\Lambda} = \frac{\left(V_{pl} - V_{fl}\right)}{3.53}. \tag{13}$$

A hyperbolic-tangent fit, described in Appendix B, is used to estimate the value of V_{pl}. In Fig. 9, we compare the temperature

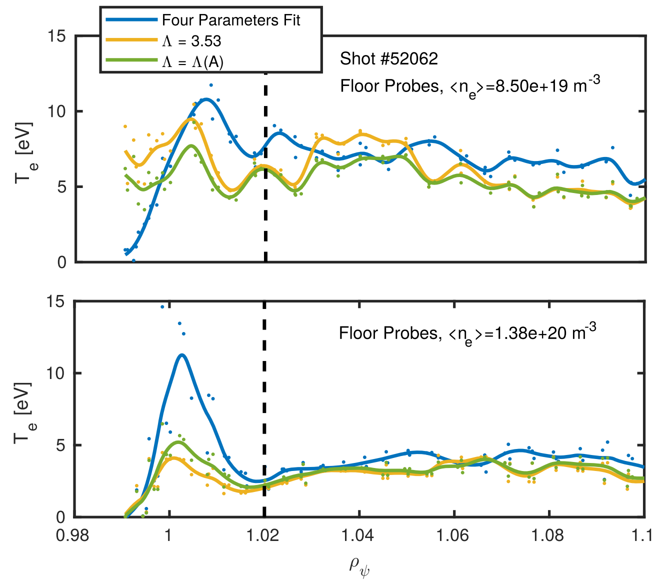

FIG. 9. Temperature profiles at $\langle n_e \rangle \approx 8.50 \times 10^{19}$ m^{-3} and $\langle n_e \rangle \approx 1.38 \times 10^{20}$ m^{-3} for the shot presented in Figs. 2 and 5 using either the four-parameter fit [Eq. (1)], Eq. (13), or using the A dependence of Λ described in Fig. 12. A was estimated using the hyperbolic tangent fit presented in Appendix B and is comprised between ≈3 and 4 in this case.

profiles of Fig. 8 at $\langle n_e \rangle \approx 8.50 \times 10^{19}$ m^{-3} and $\langle n_e \rangle \approx 1.38 \times 10^{20}$ m^{-3}, obtained with the four-parameter fit, with the ones determined from Eq. (13), assuming $\Lambda = 3.5$. Before detachment, at $\langle n_e \rangle \approx 8.50 \times 10^{19}$ m^{-3}, we observe fairly good agreement between the two methods. However, after detachment ($\langle n_e \rangle \approx 1.38 \times 10^{20}$ m^{-3}), a temperature peak is observed with the four-parameter fit, around $\rho_\psi \approx 1$, while it is much less pronounced with the temperature estimated from Eq. (13). In the top panel of Fig. 10, we have plotted the I-V characteristics associated with two probes contributing to the temperature profile plotted in Figs. 8 and 9 at $\langle n_e \rangle \approx 1.38 \times 10^{20}$ m^{-3}. Probe 4, located near the strike point ($\rho_\psi \approx 1$), shows a temperature of about 10 eV. Conversely, probe 11, which is away from the strike point, shows a temperature of about 3.5 eV. The quantity $\Lambda = \left(V_{pl} - V_{fl}\right)\frac{1}{T_e}$ is represented for both I-V curves, with V_{fl} and T_e estimated from the four-parameter fit. In the bottom panel of 10, Λ is plotted as a function of time for the same probes. While probe 11 keeps an approximately constant value of Λ, around 3 (not far from the expected theoretical value), probe 4 shows an erratic behavior with significant differences with the expected value.

Let us denote with $E_{sat} = I_{pr}\left(V_{pr} > V_{pl}\right)$ the electron saturation current. We see in the top panels of Fig. 10 that the value of Λ and the ratio $\kappa = |E_{sat}/I_{sat}|$ of electron to ion saturation current differ substantially for the two probes. The model presented so far allows us to compute the expected value of κ. When the plasma potential is reached by the probe, there is no sheath anymore and the electron current reaching the probe corresponds to the flux resulting from a Maxwellian distribution. Similarly, the ion current reaching the probe in these conditions will correspond to the flux resulting from a Maxwellian distribution of temperature T_i. The theoretical

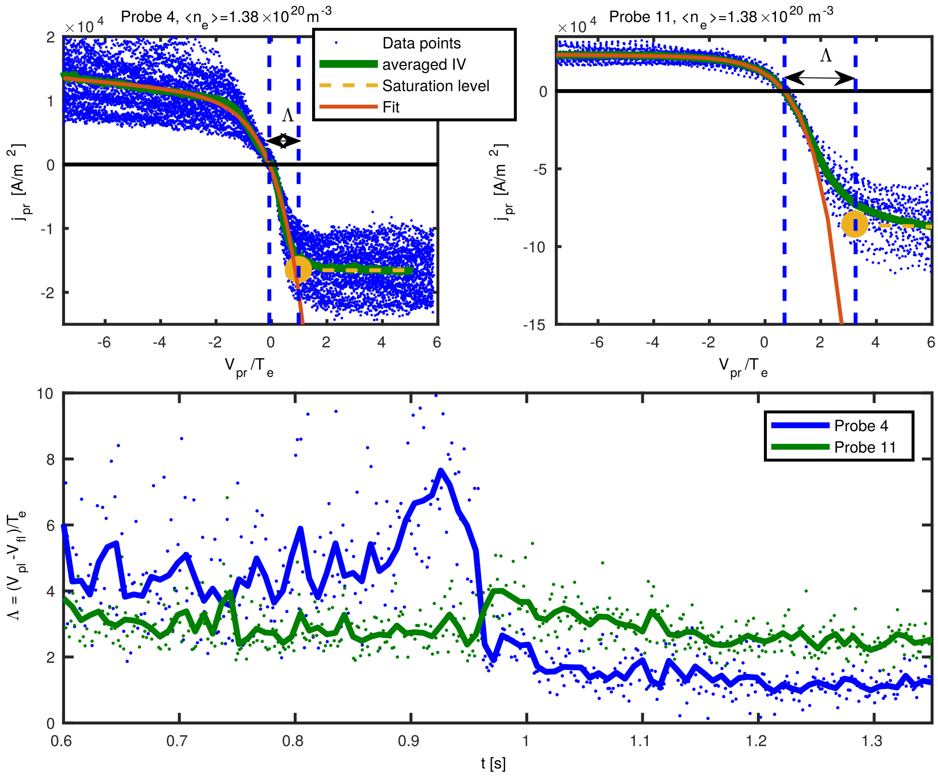

FIG. 10. (Top) Averaged I-V curve and associated fit for probes 4 (left) and 11 (right) at $\langle n_e \rangle \approx 1.38 \times 10^{20}$ m^{-3}. The voltages are normalized to the temperature determined at this time by the four-parameter fit for each probe. Probe 4 is one of the contributors to the temperature peak plotted in Fig. 8, while probe 11 does not exhibit this behavior. The yellow dashed line indicates the level of the electron current saturation, while the yellow dot indicates the position of the first point where saturation is determined by the modified hyperbolic tangent function, Appendix B. The solid black line indicates the level $j_{pr} = I_{pr}/S = 0$, and the vertical dashed lines indicates the interval $[V_{fl}/T_e, V_{pl}/T_e]$. The bottom panel shows the evolution of $\Lambda = (V_{pl} - V_{fl})/T_e$ over time for these two different probes. Again, T_e has been estimated using the four-parameter fit.

current reaching the probe at $V_{pr} = V_{pl}$ can then be written as[1]

$$I_{pr}^{th}\left(V_{pr} = V_{pl}\right) = Se\left(\frac{1}{4}\sqrt{\frac{8T_i}{\pi m_i}} - \frac{1}{4}\sqrt{\frac{8T_e}{\pi m_e}}\right) \times 2n_{se}, \qquad (14)$$

$$= -I_{sat}e^{\Lambda}\left(1 - \sqrt{\frac{T_i}{T_e}}\sqrt{\frac{m_e}{m_i}}\right). \qquad (15)$$

For $T_i = T_e$, we thus have $I_{pr}^{th}\left(V_{pr} = V_{pl}\right) \approx -I_{sat}e^{\Lambda}$. If one computes only the contribution from the electrons, denoted with E_{sat}^{th}, one has

$$E_{sat}^{th} = -\frac{1}{4}\sqrt{\frac{8T_e}{\pi m_e}}Se \times 2n_{se}, \qquad (16)$$

$$= -I_{sat}\sqrt{\frac{2m_i}{\pi m_e}\left(\frac{T_e}{T_e + \gamma T_i}\right)}, \qquad (17)$$

$$= -I_{sat}e^{\Lambda}, \qquad (18)$$

and therefore the current $E_{sat}^{th} = I_{pr}^{th}\left(V_{pr} > V_{pl}\right)$ measured by a probe for $V_{pr} \geq V_{pl}$ corresponds to the electron saturation current. Moreover, one has

$$\frac{E_{sat}^{th}}{I_{sat}} = -\sqrt{\frac{2m_i}{\pi m_e}\left(\frac{T_e}{T_e + \gamma T_i}\right)} \approx -34. \qquad (19)$$

From the theory, we expect $\kappa^{th} = \left|E_{sat}^{th}/I_{sat}\right| = 34$. However, it can be seen from the I-V curves in Fig. 10 that while κ remains fairly high for probe 11, it is close to unity for probe 4. This tends to indicate that the model used so far which constitutes the basis for both the four-parameter fit and Eq. (13) might not be applicable in this situation. In the bottom panel of Fig. 11, we have plotted the evolution of κ for probe 8. The highest value of κ reached by this particular probe is about 15, well below the theoretical value. Furthermore, it appears that, as density is increased, κ decreases, indicating that the I-V characteristics tend to be closer to symmetry. We note that this behavior is reminiscent of observations on other devices such as JET,[30] where a reduction of κ is also observed in detached regimes. A possible way to interpret the decrease of κ would be to relax the hypotheses $\gamma = 1$ and $T_i = T_e$ in the computation of κ and thus of the saturation level. Values of γ are

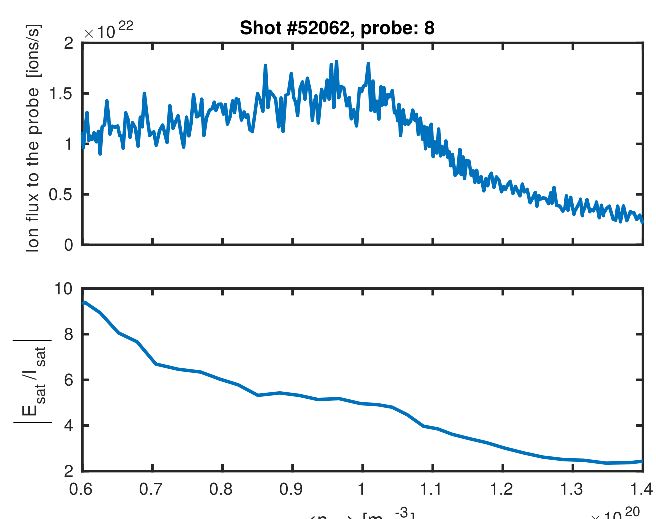

FIG. 11. (Top) Ion flux reaching LP number 8 during the density ramp. Notice the reduction of the flux after $\langle n_e \rangle \approx 1 \times 10^{19}$ m^{-3}, an indication of detachment. (Bottom) Evolution of the ratio $\left|\frac{E_{sat}}{I_{sat}}\right| = \kappa$ as a function of time. κ monotonically decreases over time, indicating that I-V curves become more symmetrical.

typically between 1 and 3 depending on the physics chosen to describe it.[1] From Eq. (19), it is possible to derive the ratio T_i/T_e that one would need to have $\kappa^{th} \approx 5$, the average value plotted in Fig. 11. Assuming $\gamma = 3$ and a deuterium plasma, one finds $T_i/T_e \approx 30$. While having ions hotter than electrons is commonly observed in the SOL,[44] we consider that such a temperature difference is unlikely, and we therefore argue that the fact that the ratio κ is lower than the one given by Eq. (19) does not only come from a possible role of ion temperature but also from other effects. One might suspect a possible role of electron self-emission by the probe itself. However, following Richardson's law,[45] this would require the probe's temperature to reach approximately 2500 K and the onset of the self-emission process would appear as a very abrupt change of the I-V characteristics,[46,47] which is in contradiction with the observations made in Fig. 11, where it appears that the reduction of κ is a continuous decay throughout the discharge.

So far, we have neglected the presence of a magnetic field, except in the evaluation of S. However, since the plasma is strongly magnetized, the charges reaching the probe will originate from the magnetic flux tube to which the probe is connected. This flux tube cannot provide more charges than it can refill, through cross-field transport or from its other end. This is known to reduce the expected value of the electron saturation current and hence κ.[4,48] A modification of the cross-field transport or of the electron mean free path during the experiment, due to the change of the plasma conditions, could explain, at least partially, the trend observed in Fig. 11.

In the following, we discuss a model that develops this idea of a particular flux tube providing charges to the probe and which reproduces a saturation of the electron current. We consider that our probe is connected, through its companion flux tube, to a particular region of the wall, which will be responsible for collecting or providing charges to the probe. In this sense, this particular area of the wall will act as a virtual electrode[30,49] (cross-field currents can be accounted for in this picture simply by artificially changing the effective area of the virtual electrode). The electron or ion currents reaching the probe will thus be limited by the ability of the virtual electrode to provide these charges, and the magnitude of the electron saturation current can thus be lower than that one would expect. In the following, we note A, the ratio between the collection area of the virtual electrode and the collection area of the probe. We assume that $A > 1$, and we denote with I_{pr} the current reaching the Langmuir probe, I_{ve} the current at the virtual electrode, V_{fl} the floating potential at the probe, and $\delta V\left(V_{pr}\right)$ the self-modification of the plasma potential in the perturbed flux tube to enforce current conservation. It is important to note that $\delta V\left(V_{pr}\right)$ is not a constant but a function of V_{pr}. The ion saturation current at the probe is denoted with I_{sat}. Because of current conservation, $I_{pr} + I_{ve} = 0$, the electron saturation current at the probe will be limited to $-AI_{sat}$. This provides a natural saturation mechanism for the I-V curve in the electron saturation part of the curve. In the following, the voltages are normalized to the temperature, $\tilde{V} = V/T_e$, and we note $\Delta\tilde{V} = \tilde{V}_{pr} - \tilde{V}_{fl}$. We can then write

$$I_{pr} = I_{sat}\left(1 - \mathrm{e}^{\Delta\tilde{V} - \delta\tilde{V}}\right), \tag{20}$$

$$I_{ve} = AI_{sat}\left(1 - \mathrm{e}^{-\delta\tilde{V}}\right). \tag{21}$$

From the current conservation $I_{pr} + I_{ve} = 0$, we have

$$1 - \mathrm{e}^{\Delta\tilde{V} - \delta\tilde{V}} = -A\left(1 - \mathrm{e}^{-\delta\tilde{V}}\right), \tag{22}$$

and thus

$$\delta\tilde{V} = \ln\left(\frac{\mathrm{e}^{\Delta\tilde{V}} + A}{1 + A}\right). \tag{23}$$

Re-injected in Eq. (20), this yields

$$I_{pr} = AI_{sat}\frac{1 - \mathrm{e}^{\Delta\tilde{V}}}{A + \mathrm{e}^{\Delta\tilde{V}}}. \tag{24}$$

However, the probe current is not allowed to reach values below $-\kappa^{th}I_{sat}$. No such limitation is imposed by Eq. (24). Therefore, we need to add a supplemental constraint enforcing the saturation of the electron current if

$$\mathrm{e}^{\Delta\tilde{V}}\left(A - \kappa^{th}\right) \geq A\left(\kappa^{th} + 1\right), \tag{25}$$

which has solutions only if $A \geq \kappa^{th}$. Thus, if $A \geq \kappa^{th}$, then Eq. (24) must be rewritten as

$$I_{pr} = \begin{cases} AI_{sat}\frac{1-\mathrm{e}^{\Delta\tilde{V}}}{A+\mathrm{e}^{\Delta\tilde{V}}} \\ -\kappa^{th}I_{sat}, \quad \text{if } A \geq \kappa^{th} \text{ and } \Delta\tilde{V} > \ln\left(\frac{A(\kappa^{th}+1)}{A-\kappa^{th}}\right) \end{cases}. \tag{26}$$

This implies that, using the previous notation, one has $\kappa = A$ if $A < \kappa^{th}$ and $\kappa = \kappa^{th}$ otherwise. In the top panel of Fig. 12 are plotted synthetic I-V curves generated using Eq. (26) for different values of A and arbitrary, but fixed, T_e, n_e, and V_{fl}. From these synthetic I-V curves, it is then possible to link the electron temperature T_e to the difference between V_{pl} and V_{fl}, thus finding the Λ function introduced before. This is done in the bottom plot of Fig. 12, where we have plotted Λ as a function of A. To do so, we evaluate V_{pl} using the tangent fit

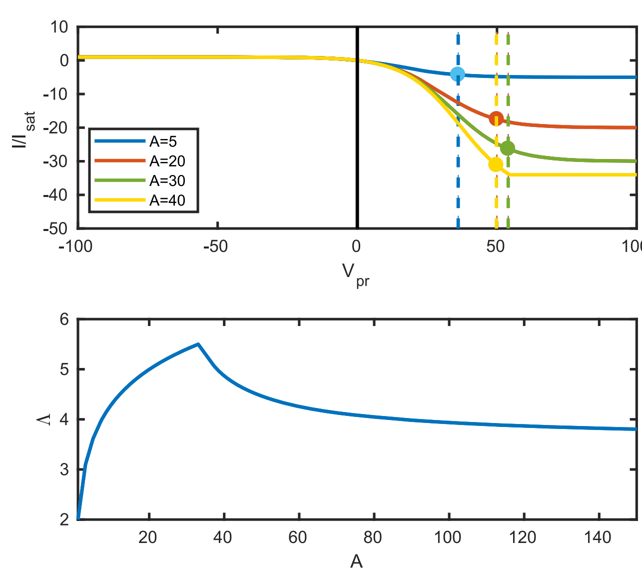

FIG. 12. (Top) Synthetic I-V curves generated from relation 26 assuming $V_{fl} = 0$ and $T_e = 10$ eV. Only A is varying. The vertical black line indicates the position of V_{fl}, while the colored vertical lines and dots indicate the position of the first saturation point, defined as the first point where the 95% of the electron saturation current is reached. (Bottom) Dependency of Λ versus A.

(Appendix B). Knowing the parameter T_e and V_{fl} that have been used to generate the synthetic I-V curves, Λ is evaluated. While not shown in Fig. 12, we retrieve in this model that for $A \to \infty$, $\Lambda = 3.53$. In Fig. 9, we have plotted the temperature derived using Eq. (13) but keeping the dependency of Λ on A. This method, which we shall refer to as the Λ-method in the remainder of this paper, yields similar temperatures than assuming $\Lambda \approx 3.5$. We also note that Eq. (26) provides a model that could, in principle, be used to fit the I-V characteristics and directly deduce the temperature. However, this model does not include the sheath expansion, whose effect on the characteristics can be important. As a result, fits done with Eq. (26) overestimate T_e and I_{sat}. Thus, in Sec. V of this paper, we extend the asymmetric double probe model by including the sheath expansion.

V. ASYMMETRIC DOUBLE PROBE MODEL WITH SHEATH EXPANSION

A. Model and implementation

In this section, we present a fitting model based on the asymmetric double probe including the effect of sheath expansion. A similar model has been developed in Ref. 18. We however introduce here a simplified formulation, and we show that the sheath expansion effect can be included in the model while keeping a semi-analytical expression for the expression, therefore facilitating its implementation and use. We start the derivation of the model with the same assumptions as for an asymmetric double probe without the sheath expansion and write

$$I_{pr} = S n_{se} c_s e \left(1 + \alpha \left(V_{pr} - \left(V_{fl} + \delta V\right)\right) - e^{\frac{V_{pr} - \left(\delta V + V_{fl}\right)}{T_e}}\right), \tag{27}$$

$$I_{ve} = A S n_{se} c_s e \left(1 - \frac{\beta}{A}\delta V - e^{\frac{-\delta V}{T_e}}\right), \tag{28}$$

where the quantities have the same meaning as in Sec. IV. We add two linear terms to describe the sheath expansion, governed by the coefficients α and β. From charge conservation, we have again $I_{pr} + I_{ve} = 0$, and therefore $\delta V\left(V_{pr}\right)$ is defined by the implicit relation

$$e^{\frac{-\delta V}{T_e}}\left(A + e^{\frac{V_{pr} - V_{fl}}{T_e}}\right) + (\alpha + \beta)\,\delta V - \left(1 + A + \alpha\left(V_{pr} - V_{fl}\right)\right) = 0. \tag{29}$$

This equation is of the form $ae^x + bx + c$. For $\alpha + \beta < 0$, and following Appendix A, we can show that Eq. (29) has exactly one solution, given by

$$\delta V = -T_e\left[-W_0(\Delta) - \frac{1 + A + \alpha\left(V_{pr} - V_{fl}\right)}{T_e(\alpha + \beta)}\right], \tag{30}$$

where W_0 is the 0-th branch of the Lambert W function, and Δ is defined as

$$\Delta = -\frac{A + e^{\frac{V_{pr} - V_{fl}}{T_e}}}{T_e(\alpha + \beta)} e^{\frac{1 + A + \alpha\left(V_{pr} - V_{fl}\right)}{-T_e(\alpha + \beta)}}. \tag{31}$$

Since the current conservation $I_{pr} + I_{ve} = 0$ holds, by construction, for every value of V_{pr}, and since I_{ve} is bounded to AI_{sat} (assuming $A < \kappa^{th}$), then I_{pr} will saturate to $-AI_{sat}$ for $V_{pr} \gg V_{pl}$. We now show that for $V_{pr} = V_{fl}$, we have $\delta V = 0$ and thus $I_{pr}\left(V_{pr} = V_{fl}\right) = 0$, as it should. From Eq. (30), if $V_{pr} = V_{fl}$, we find

$$\Delta = -\frac{A + 1}{T_e(\alpha + \beta)} e^{-\frac{A+1}{T_e(\alpha + \beta)}}, \tag{32}$$

using the fact that, by the definition of the Lambert function W, one has $W(xe^x) = x$, we have

$$-W_0(\Delta) = \frac{A + 1}{T_e(\alpha + \beta)}, \tag{33}$$

which yields, using Eq. (30),

$$\delta V\left(V_{pr} = V_{fl}\right) = 0. \tag{34}$$

Therefore, from Eq. (27), we have $I_{pr}\left(V_{pr} = V_{fl}\right) = 0$ and V_{fl} is indeed the floating potential at the probe location.

Unlike the four-parameter fit, this method can be used to fit the entire of the I-V curve. Six parameters have to be fitted: I_{sat}, T_e, V_{fl}, A, α, and β, where $I_{sat} = S n_{se} c_s e$. $\delta V\left(V_{pr}\right)$ is evaluated either by using Eq. (30) or by finding the zero of Eq. (29), thanks to Newton's method or a Powell hybrid method provided by the routine HYBRD of MINPACK. All the three methods yields similar results, and the analytical evaluation of δV using Eq. (29) is chosen as the default one since it is faster. For the fitting in itself, we adopt a three-step method. Using a hyperbolic tangent fit (Appendix B), the parameters α and β are first estimated. I_{sat}, T_e, V_{fl}, and A are then estimated using Eqs. (27) and (29), holding α and β constant. In the second step, based on the estimated values of I_{sat}, T_e, V_{fl}, and A, we fit the model to estimate α and β. Finally, in a third and last step, we perform a fit with the 6 parameters I_{sat}, T_e, V_{fl}, A, α, and β using the values estimated in the previous steps as a starting point. This three-step method yields the same results as the direct 6 parameter fit but appears to produce less outliers. It is important to remark that as this fit uses the entire I-V characteristic, it is sensitive to the saturation of the electronics if the electron saturation current amplitude is particularly high.

In Fig. 13, we have plotted the fit performed on a single I-V curve, as well as the fit obtained when using an averaged I-V curve obtained from a 50 ms aggregation of data. As one can see, this model is able to adequately fit the electron current saturation part of the characteristic and thus does not require the need for an additional criterion such as the minimum temperature approach used for the four-parameter fit. It however requires the electron saturation part of the characteristic to be well measured to be able to provide a reliable fit. For high values of κ reached, for instance, in *attached* (i.e., non-detached) conditions, it can happen that the electron branch has such a high amplitude that it leads to a saturation of the measurements. In that case, the electron saturation current is not properly captured by our measurements, and thus, this fit cannot be applied. Figure 14 shows the temperature profiles resulting from analysis using the asymmetric double probe fit, compared to the profiles obtained previously in Fig. 8 with the four-parameter fit, for the lowest and highest densities plotted in Fig. 5. In the low density case, probes 6–10 had to be excluded from the analysis as they corresponded to saturated

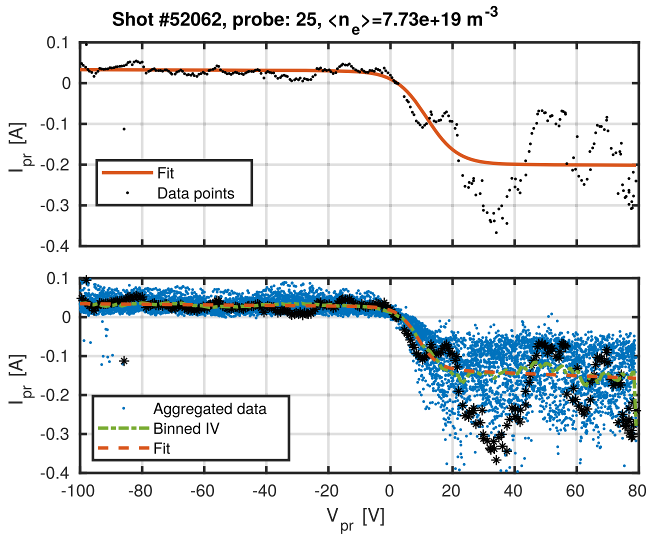

FIG. 13. The same data as in Fig. 5, but now analyzed using the asymmetric double probe fit. The color code is the same as in Fig. 5.

measurements and thus were unsuitable for fitting. For the remaining probes, the temperatures determined by both fits are similar. In the high density case, all probes could be kept in the analysis. Indeed, the lower amplitude of the electron saturation in detached conditions allows us to have a good description of this part of the curve. It is clear from Fig. 14 that the asymmetric double probe fit leads to lower temperature. Furthermore, the strong peaking observed previously near the strike-point is not observed, a possible indication that this fit is more reliable, thanks to its ability to fit the entire I-V characteristic. However, the temperatures that are measured remain fairly high (∼5 eV) near the strike-point where

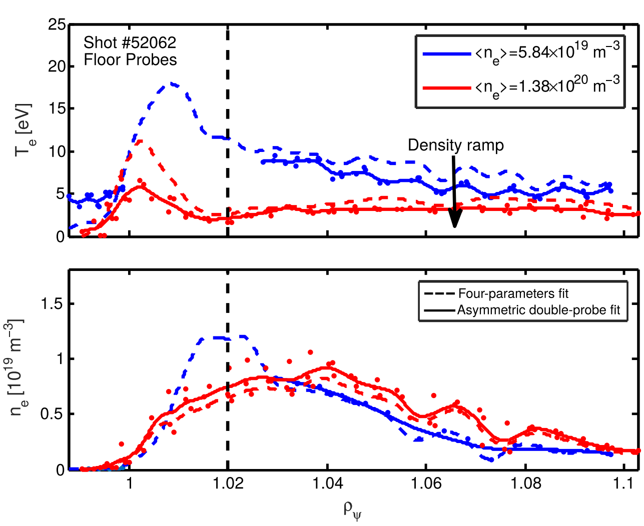

FIG. 14. Temperature (top) and density (bottom) profiles measured by the floor probes for the same discharge as in Fig. 8 and for the lowest density and highest density. The asymmetric double probe fit with the sheath expansion is used to determine T_e and n_e. In the low density case, probe 6–10 had to be excluded from the analysis as their electron saturation branches were poorly resolved. For reference, the profiles obtained with the four-parameter fit in Fig. 8 are plotted as well (dashed lines).

we would expect from detachment physics significantly lower temperatures. This possible over-estimation of the temperature by the probes is interpreted as a signature of the presence of kinetic effects.[14] Thus, in the following part, we investigate the sensitivity of our different fitting models (four-parameter, asymmetric double probe, Λ-method) toward the existence of a population of fast electrons.

VI. POSSIBLE INFLUENCE OF FAST ELECTRONS ON THE MEASURED TEMPERATURE

Previous analysis relies on the assumption that the electron distribution is Maxwellian, which is not necessarily the case. For instance, there could be a population of fast electrons, characterized by a hotter temperature than the bulk population. This has been predicted in tokamaks,[14,40,50] in particular, after detachment.[14] It has been confirmed experimentally in the CASTOR (*Czech Academy of Sciences TORus*)[51] and NSTX (*National Spherical Torus Experiment*)[42,52] tokamaks, where non-Maxwellian distribution functions have been observed. In Ref. 51, in particular, it has been seen that the electron distribution is not Maxwellian but can be approximated by a bi-Maxwellian distribution with a bulk of low temperature electrons and a second population of hot electrons since these hotter electrons will tend to contribute more to the I-V electron current than the cold ones, especially around and below the floating potential. Therefore, already for a relatively low fraction of the hot population, the temperature inferred from the standard analysis no longer represents the temperature of the bulk population. In this part, we evaluate the robustness of the different fitting methods in the presence of fast electrons. We proceed in a way very similar to Ref. 40. For simplicity, we assume that the electron distribution function consists of the superposition of two Maxwellian populations of electrons that coexist in our plasma: a population of "slow" electrons at a temperature $T_{e,s}$ and of density $n_{e,s}$, and a population of "fast" electrons at a temperature $T_{e,f}$ and of density $n_{e,f}$. We consider a Langmuir probe maintained at a potential V_{pr} and denote with V_{se} the sheath-edge potential at floating conditions. We define $h = n_{e,f}/n_{e,s}$ and $r = n_{e,f}/(n_{e,f} + n_{e,s}) = h/(1 + h)$ which quantifies the fraction of fast electrons over the total electron population. The temperature ratio of the electron populations is defined by $g = \frac{T_{e,f}}{T_{e,s}}$. One can then write the electron flux Γ_e as

$$\Gamma_e = \frac{1}{4} n_{e,s}\overline{c_{e,s}}\left[e^{\frac{V_{pr}-V_{se}}{T_{e,s}}} + h\sqrt{g}\,e^{\frac{V_{pr}-V_{se}}{T_{e,f}}}\right], \qquad (35)$$

where $\overline{c_{e,s}} = \sqrt{\frac{8T_{e,s}}{\pi m_e}}$. Noting n_{se} as the electron density at the sheath edge, we have $n_{e,s}(1 + h) = n_{se}$. The ion flux Γ_i is defined as $\Gamma_i = n_{se}c_s$, where assuming $\gamma = 1$,

$$c_s = \sqrt{\frac{(T_i + fT_{e,s})}{m_i}} \qquad (36)$$

with $f = g\frac{(1+h)}{(h+g)}$ (see Ref. 53). Since at the floating potential V_{fl} one has $\Gamma_i = \Gamma_e$, V_{fl} is the solution of

$$\sqrt{\frac{8m_i}{\pi m_e}\frac{T_{e,s}}{T_i+fT_{e,s}}}=4\frac{(1+h)}{\left[e^{\frac{V_{fl}-V_{se}}{T_{e,s}}}+h\sqrt{g}e^{\frac{V_{fl}-V_{se}}{T_{e,f}}}\right]}. \tag{37}$$

As for the ion temperature T_i, we assume $T_i = fT_{e,s}$ for simplicity. This yields $T_i \to T_{e,s}$ for $h \to 0$ and $T_i \to T_{e,f}$ for $h \to \infty$. In typical conditions where one expects the slow electrons to be the majority, $h \ll 1, f \approx 1$, and $T_i \approx T_{e,s}$. We also define $\Delta = V_{se} - V_{fl}$ such that Eq. (37) reads

$$\sqrt{\frac{8m_i}{2\pi m_e f}}=4\frac{(1+h)}{\left[e^{\frac{-\Delta}{T_{e,s}}}+h\sqrt{g}e^{\frac{-\Delta}{T_{e,f}}}\right]}. \tag{38}$$

This equation is used to determine Δ and thus the floating potential if the voltage at the sheath entrance is taken as the reference. The current reaching the probe then reads $I_{pr} = S\,(e\Gamma_i - e\Gamma_e)$, where S is the collection area of the probe. I_{pr} can be rewritten as

$$I_{pr}=I_{sat}\left(1-\frac{e^{\frac{V_{pr}-V_{se}}{T_{e,s}}}+h\sqrt{g}e^{\frac{V_{pr}-V_{se}}{T_{e,f}}}}{\left[e^{\frac{-\Delta}{T_{e,s}}}+h\sqrt{g}e^{\frac{-\Delta}{T_{e,f}}}\right]}\right), \tag{39}$$

where $I_{sat} = eSn_{se}c_s = eSn_{se}\sqrt{\frac{(T_i+fT_{e,s})}{m_i}}$. It should be noted that, in our model, I_{sat} depends on the population of fast electrons since c_s depends on f and T_i, the latter also depending on f. We now use the asymmetric double probe model that was presented in Sec. IV. The electron or ion currents reaching the probe will thus be limited by the ability of a virtual electrode to provide these charges. We use the same notations and definitions as in Sec. IV. Because of current conservation $I_{pr} + I_{ve} = 0$, the current density reaching the probe can be written as

$$I_{pr}=I_{sat}\left(1-\frac{e^{\frac{V_{pr}-(\Delta+\delta V+V_{fl})}{T_{e,s}}}+h\sqrt{g}e^{\frac{V_{pr}-(\Delta+\delta V+V_{fl})}{T_{e,f}}}}{\left[e^{\frac{-\Delta}{T_{e,s}}}+h\sqrt{g}e^{\frac{-\Delta}{T_{e,f}}}\right]}\right), \tag{40}$$

where we did not include the effect of sheath expansion for the sake of simplicity. If we assume that the fast electron population is the same in front of the probe and the virtual electrode, the current at the electrode can be written as

$$I_{ve}=AI_{sat}\left(1-\frac{e^{\frac{-(\Delta+\delta V)}{T_{e,s}}}+h\sqrt{g}e^{\frac{-(\Delta+\delta V)}{T_{e,f}}}}{\left[e^{\frac{-\Delta}{T_{e,s}}}+h\sqrt{g}e^{\frac{-\Delta}{T_{e,f}}}\right]}\right). \tag{41}$$

Thus, proceeding in the same way as in Sec. IV and invoking current conservation, $\delta V(V_{pr})$ is defined by the implicit relation $I_{pr} + I_{ve} = 0$. As for Eq. (27), one can now check that V_{fl} is indeed the floating potential, i.e., $I_{pr}\left(V_{pr} = V_{fl}\right) = 0$. For $V_{pr} = V_{fl}$ and $\delta V = 0$, one finds $I_{pr} = I_{ve} = 0$ and $I_{pr}(V_{pr} = V_{fl}) + I_{ve}(V_{pr} = V_{fl}) = 0$. Since $I_{pr}(V_{pr} = V_{fl}) + I_{ve}(V_{pr} = V_{fl})$ is a monotonous function of δV, it ensures that $\delta V = 0$ is the unique solution that enforces $I_{pr} + I_{ve} = 0$ at $V_{pr} = V_{fl}$, and we thus indeed have $I_{pr}(V_{pr} = V_{fl}) = 0$.

In Fig. 15, we have plotted a set of I-V curves generated from this expression for different values of r. For the purpose of the plot, $T_{e,f} = 10$ eV, $T_{e,s} = 2$ eV, $A = 5$, and $V_{fl} = 1$ V

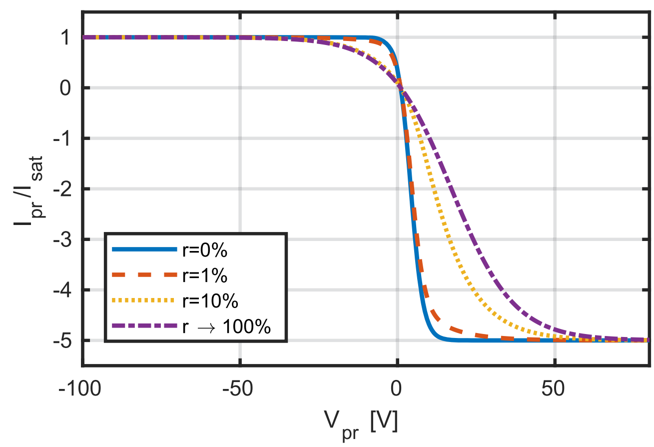

FIG. 15. Synthetic I-V curves generated using Eq. (40) for different values of the fast electron population density, quantified by $r = n_{e,f}/(n_{e,f} + n_{e,s})$. The cold electrons are at $T_{e,s} = 2$ eV and the fast ones at $T_{e,f} = 10$ eV. The ratio of the saturation currents is given by $A = 5$.

were assumed. One can see that an increase in the fast electron population is associated with a broadening of the I-V characteristics, which relatively quickly lead to the measurement of a temperature higher than the one set by the cold electron population. Values of r as low as 1% are already strong enough to have a visible impact on the characteristic. This is reflected on the temperature derived from the different fits, as shown in Fig. 16, where the temperatures derived with the different methods presented in this paper are represented as a function of r. For low values of r, the impact of the fast electron population is small and the temperature is correctly determined by the different fits. However, as r increases, the different fits start to get influenced by the presence of the fast electron population and return a temperature substantially larger than that of the bulk, even for r as low as 5%. In Fig. 16, we have also plotted with a dashed line the results obtained assuming a larger ratio of the ion to electron saturation currents, $A = 15$. While the

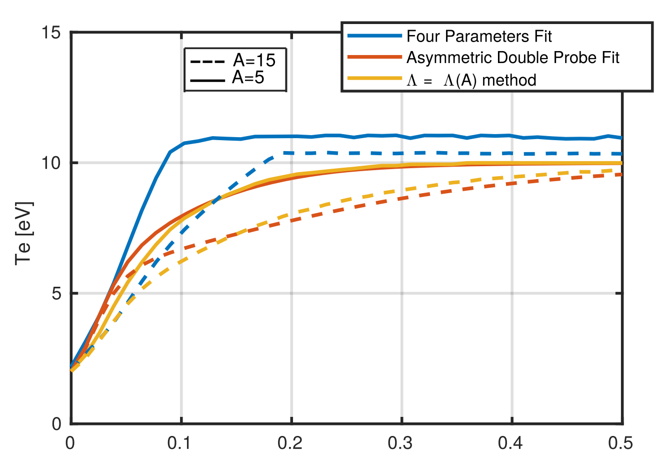

FIG. 16. Temperatures determined from fitting the synthetic I-V curves presented in Fig. 15 ($A = 5$) for different concentrations r of fast electrons. The temperatures determined from similar I-V curves, generated using $A = 15$, are also plotted using dashed lines. (For the color version of this figure, the reader is referred to the online version of this article).

temperatures estimated by the fits are higher than the temperature of the cold electron population, the "over-estimation" is not as strong as for a lower value of A. This illustrates how the reduction of this ratio, observed in detached plasmas, increases the sensitivity of our analysis workflow to the presence of fast electrons. For both values of A, it appears that the asymmetric double probe fit and the Λ-method have a very similar sensitivity, while the four-parameter fit is more sensitive toward the presence of fast electrons for low values of A, typical for detached conditions. For larger values of A and low values of r, the situation reverses and the four-parameter fit appears to provide a lower estimate of the temperature than the asymmetric double probe fit. This is not surprising, as for large values of A, Eq. (24) tends toward Eq. (1). But since the four-parameter fit is coupled to a minimum temperature approach, it is biased toward deriving low temperatures. Overall, it appears that all fits are very sensitive toward the presence of fast electrons and that they cannot estimate the temperature of the bulk population even for moderate presence of fast electrons. This could explain, at least partially, the apparent over-estimation of temperature at detachment. The fact that the four-parameter fit is more sensitive than the asymmetric double probe fit to the fast electrons could also explain in part why it leads to a peaking of the temperature in detached conditions (where A is low).

VII. CONCLUSION

This paper presents the standard method used to analyze current-voltage characteristics of the wall-embedded Langmuir probes on the TCV tokamak and the strategies deployed in order to improve the measurements in the detached regime. After describing the TCV Langmuir probe system, the analysis tool chain developed to process the acquired data has been discussed in detail. It starts by removing stray currents from the signals, using a few voltage sweeps performed after the termination of the plasma. Once cleaned, the measurements are analyzed using a four-parameter fit combined with a minimum temperature method, which is the default method at TCV for the analysis of the I-V curves. The averaging process used to reduce the plasma fluctuations and noise affecting the I-V curve has been compared to analysis performed without I-V curves averaging, showing agreement between the two methods in stationary plasma conditions. We briefly described a possible way to perform analysis in non-stationary conditions, for instance, in the presence of ELMs. We also provided an estimate of the error induced by the presence of resistance in the circuitry and highlighted both computationally and analytically that a large overestimation of the temperature can occur in high density, low temperature plasmas. We then applied the analysis to experiments in the detached plasma regime, which constitutes a challenging regime of operation for the Langmuir probes. We have evidenced that the temperature profiles derived from the four-parameter fit analysis are not always reliable, in particular, close to the strike-point. Thus, two alternative methods to determine the electron temperature from the I-V curve have been presented. The first one relies on the link between the plasma potential, the floating potential, and the electron temperature. The second one is based on an asymmetric double probe model. We introduced a variant of the asymmetric double probe fit[18] that can be expressed with a semi-analytical formula. We have shown that in attached conditions, both methods yield results in agreement with the four-parameter fit, while they find lower temperatures in detached regime. In particular, the temperature peak observed near the strike point with the four-parameter fit is strongly reduced with these two methods, a sign of their robustness. However, the computed temperatures still remain higher than expected from spectroscopic measurements,[35–37] Thomson scattering,[38] or simulations. Thus in the last part, we explored the possible role that fast electrons, often considered as a possible responsibility for this discrepancy,[14] could have on the temperature measured by the Langmuir probes. We found that the two alternative methods, which rely on a larger part of the I-V curve, are only marginally less sensitive to the presence of a fast electron population. It should be noted that other effects could also be responsible for the large temperatures observed in detached conditions with the Langmuir probes, such as a modification of the plasma resistance[1,39] or the fluctuations of the floating potential.[39] These effects have not been addressed in this paper.

To summarize, by exploring three different fitting methods, we have shown that while in attached conditions the good agreement between the three methods indicates that the temperatures we determine are robust, and the discrepancies observed in detached conditions and the strong sensitivity of the analysis on a potential supra-thermal electron population call for caution in the interpretation of the inferred electron temperatures and densities.

ACKNOWLEDGMENTS

This work was supported in part by the Swiss National Science Foundation. This work has been carried out within the framework of the EUROfusion Consortium and has received funding from the Euratom research and training programme 2014-2018 under Grant Agreement No. 633053. The views and opinions expressed herein do not necessarily reflect those of the European Commission.

APPENDIX A: THE LAMBERT W FUNCTION

For $w, z \in \mathbb{C}$, the Lambert W function[27,28] is defined such that

$$z = w\mathrm{e}^{w} \iff w = W(z). \tag{A1}$$

In this appendix, we show how it can be used to solve equations of the form

$$a\mathrm{e}^{x} + bx + c = 0, \tag{A2}$$

where $(a, b) \in \mathbb{R}^{*2}$ and $(c, x) \in \mathbb{R}$. Under these assumptions, Eq. (A2) can be recasted in the form

$$\left(-x - \frac{c}{b}\right)\mathrm{e}^{-x-\frac{c}{b}} = \frac{a}{b}e^{-\frac{c}{b}}. \tag{A3}$$

Denoting $X = \left(-x - \frac{c}{b}\right)$ and $\Delta = \frac{a}{b}e^{-\frac{c}{b}}$, one has

$$X\mathrm{e}^{X} = \Delta. \tag{A4}$$

Since in this paper we restrict ourselves (by a proper choice of hypotheses) to cases where $\Delta \in \mathbb{R}$ and $\Delta > 0$, we have existence and unicity of X, leading to

$$x = -W_0(\Delta) - \frac{c}{b}, \tag{A5}$$

where W_0 is the 0-th branch of the Lambert W function.

APPENDIX B: HYPERBOLIC TANGENT FIT

In this appendix, we present the hyperbolic tangent fit that is used in the analysis chain to get an estimate of certain parameters. This fit, which is similar to the function presented in Ref. 54 to fit pedestal profiles, can be written as

$$\begin{aligned} I_{pr} = B + h \tanh\left(\frac{V_0 - V_{pr}}{d}\right) \\ + m_1 \left(V_0 - V_{pr} - d\right) \Theta \left(V_0 - V_{pr} - d\right) \\ - m_2 \left(-V_0 + V_{pr} - d\right) \Theta \left(-V_0 + V_{pr} - d\right), \end{aligned} \tag{B1}$$

where Θ is the Heaviside function and B, h, d, V_0, m_1, and m_2 are the fitting variables. m_1 and m_2 are related to the sheath parameters αI_{sat} and $\beta I_{sat}/A$ that are defined in this paper and thus can be used as initial first guesses for them. Similarly, h and B are related to A and d, which quantifies the width of the tanh part of the curve, and can be related to T_e. However, unlike other fitting models presented in this paper, this fit is not established on the basis of a physical model of the I-V characteristics and, therefore, cannot be used to derive directly the physical parameters. From Eq. (B1), the electron saturation voltage is determined as

$$V_{sat} \approx V_0 + d. \tag{B2}$$

Making the assumption that this saturation voltage does indeed correspond to the plasma potential, we therefore have

$$V_{pl} \approx V_{sat} \approx V_0 + d. \tag{B3}$$

[1] P. Stangeby, *The Plasma Boundary of Magnetic Fusion Devices*, Series in Plasma Physics and Fluid Dynamics (Taylor & Francis, 2000).

[2] K. U. Riemann, J. Phys. D: Appl. Phys. **24**, 493 (1991).

[3] H. M. Mott-Smith and I. Langmuir, Phys. Rev. **28**, 727 (1926).

[4] I. Hutchinson, *Principles of Plasma Diagnostics* (Cambridge University Press, 2005).

[5] F. Hofmann, J. B. Lister, W. Anton, S. Barry, R. Behn, S. Bernel, G. Besson, F. Buhlmann, R. Chavan, M. Corboz, M. J. Dutch, B. P. Duval, D. Fasel, A. Favre, S. Franke, A. Heym, A. Hirt, C. Hollenstein, P. Isoz, B. Joye, X. Llobet, J. C. Magnin, B. Marletaz, P. Marmillod, Y. Martin, J. M. Mayor, J. M. Moret, C. Nieswand, P. J. Paris, A. Perez, Z. A. Pietrzyk, R. A. Pitts, A. Pochelon, R. Rage, O. Sauter, G. Tonetti, M. Q. Tran, F. Troyon, D. J. Ward, and H. Weisen, Plasma Phys. Controlled Fusion **36**, B277 (1994).

[6] S. Coda, J. Ahn, R. Albanese, S. Alberti, E. Alessi, S. Allan, H. Anand, G. Anastassiou, Y. Andrèbe, C. Angioni, M. Ariola, M. Bernert, M. Beurskens, W. Bin, P. Blanchard, T. Blanken, J. Boedo, T. Bolzonella, F. Bouquey, F. Braunmüller, H. Bufferand, P. Buratti, G. Calabró, Y. Camenen, D. Carnevale, F. Carpanese, F. Causa, R. Cesario, I. Chapman, O. Chellai, D. Choi, C. Cianfarani, G. Ciraolo, J. Citrin, S. Costea, F. Crisanti, N. Cruz, A. Czarnecka, J. Decker, G. D. Masi, G. D. Tommasi, D. Douai, M. Dunne, B. Duval, T. Eich, S. Elmore, B. Esposito, M. Faitsch, A. Fasoli, N. Fedorczak, F. Felici, O. Février, O. Ficker, S. Fietz, M. Fontana, L. Frassinetti, I. Furno, S. Galeani, A. Gallo, C. Galperti, S. Garavaglia, I. Garrido, B. Geiger, E. Giovannozzi, M. Gobbin, T. Goodman, G. Gorini, M. Gospodarczyk, G. Granucci, J. Graves, R. Guirlet, A. Hakola, C. Ham, J. Harrison, J. Hawke, P. Hennequin, B. Hnat, D. Hogeweij, J.-P. Hogge, C. Honoré, C. Hopf, J. Horáček, Z. Huang, V. Igochine, P. Innocente, C. I. Schrittwieser, H. Isliker, R. Jacquier, A. Jardin, J. Kamleitner, A. Karpushov, D. Keeling, N. Kirneva, M. Kong, M. Koubiti, J. Kovacic, A. Krämer-Flecken, N. Krawczyk, O. Kudlacek, B. Labit, E. Lazzaro, H. Le, B. Lipschultz, X. Llobet, B. Lomanowski, V. Loschiavo, T. Lunt, P. Maget, E. Maljaars, A. Malygin, M. Maraschek, C. Marini, P. Martin, Y. Martin, S. Mastrostefano, R. Maurizio, M. Mavridis, D. Mazon, R. McAdams, R. McDermott, A. Merle, H. Meyer, F. Militello, I. Miron, P. M. Cabrera, J.-M. Moret, A. Moro, D. Moulton, V. Naulin, F. Nespoli, A. Nielsen, M. Nocente, R. Nouailletas, S. Nowak, T. Odstrčil, G. Papp, R. Papřok, A. Pau, G. Pautasso, V. P. Ridolfini, P. Piovesan, C. Piron, T. Pisokas, L. Porte, M. Preynas, G. Ramogida, C. Rapson, J. J. Rasmussen, M. Reich, H. Reimerdes, C. Reux, P. Ricci, D. Rittich, F. Riva, T. Robinson, S. Saarelma, F. Saint-Laurent, O. Sauter, R. Scannell, C. Schlatter, B. Schneider, P. Schneider, R. Schrittwieser, F. Sciortino, M. Sertoli, U. Sheikh, B. Sieglin, M. Silva, J. Sinha, C. Sozzi, M. Spolaore, T. Stange, T. Stoltzfus-Dueck, P. Tamain, A. Teplukhina, D. Testa, C. Theiler, A. Thornton, L. Tophøj, M. Tran, C. Tsironis, C. Tsui, A. Uccello, S. Vartanian, G. Verdoolaege, K. Verhaegh, L. Vermare, N. Vianello, W. Vijvers, L. Vlahos, N. Vu, N. Walkden, T. Wauters, H. Weisen, M. Wischmeier, P. Zestanakis, M. Zuin, and EUROfusion MST1 Team, Nucl. Fusion **57**, 102011 (2017).

[7] J. P. Gunn, C. Boucher, B. L. Stansfield, and S. Savoie, Rev. Sci. Instrum. **66**, 154 (1995).

[8] R. Dejarnac, J. P. Gunn, J. Stöckel, J. Adámek, J. Brotánková, and C. Ionita, Plasma Phys. Controlled Fusion **49**, 1791 (2007).

[9] C. Theiler, I. Furno, A. Kuenlin, P. Marmillod, and A. Fasoli, Rev. Sci. Instrum. **82**, 013504 (2011).

[10] M. Bagatin, D. Desideri, E. Martines, G. Manduchi, G. Serianni, and V. Antoni, Rev. Sci. Instrum. **68**, 365 (1997).

[11] H. Zohm, Plasma Phys. Controlled Fusion **38**, 105 (1996).

[12] A. W. Leonard, Plasma Phys. Controlled Fusion **60**, 044001 (2018).

[13] C. Theiler, B. Lipschultz, J. Harrison, B. Labit, H. Reimerdes, C. Tsui, W. A. J. Vijvers, J. A. Boedo, B. P. Duval, S. Elmore, P. Innocente, U. Kruezi, T. Lunt, R. Maurizio, F. Nespoli, U. Sheikh, A. J. Thornton, S. H. M. van Limpt, K. Verhaegh, N. Vianello, TCV Team, and EUROfusion MST1 Team, Nucl. Fusion **57**, 72008 (2017).

[14] O. V. Batishchev, S. I. Krasheninnikov, P. J. Catto, A. A. Batishcheva, D. J. Sigmar, X. Q. Xu, J. A. Byers, T. D. Rognlien, R. H. Cohen, M. M. Shoucri, and I. P. Shkarofskii, Phys. Plasmas **4**, 1672 (1997).

[15] R. Pitts, S. Alberti, P. Blanchard, J. Horacek, H. Reimerdes, and P. Stangeby, Nucl. Fusion **43**, 1145 (2003).

[16] S. A. Self, Phys. Fluids **6**, 1762 (1963).

[17] E. Zawaideh, F. Najmabadi, and R. W. Conn, Phys. Fluids **29**, 463 (1986).

[18] M. Weinlich and A. Carlson, Phys. Plasmas **4**, 2151 (1997).

[19] J.-M. Moret, B. Duval, H. Le, S. Coda, F. Felici, and H. Reimerdes, Fusion Eng. Des. **91**, 1 (2015).

[20] J. P. Gunn, C. Boucher, B. L. Stansfield, and C. S. Maclatchy, Contrib. Plasma Phys. **36**, 45 (1996).

[21] U. Wolters, T. Daube, K.-U. Riemann, and K. Wiesemann, Plasma Phys. Controlled Fusion **41**, 721 (1999).

[22] C. K. Tsui, J. A. Boedo, P. C. Stangeby, and TCV Team, Rev. Sci. Instrum. **89**, 013505 (2018).

[23] I. Furno, F. Avino, A. Bovet, A. Diallo, A. Fasoli, K. Gustafson, D. Iraji, B. Labit, J. Loizu, S. H. Müller *et al.*, J. Plasma Phys. **81**, ■ (2015).

[24] J. J. Moré, B. S. Garbow, and K. E. Hillstrom, ANL-80-74, Argonne National Laboratory, 1980.

[25] J. J. Moré, D. C. Sorensen, K. E. Hillstrom, and B. S. Garbow, *The MINPACK Project, in Sources and Development of Mathematical Software* (Prentice-Hall, Inc., Upper Saddle River, NJ, USA, 1984), pp. 88–111.

[26] J. Stillerman and T. W. Fredian, Fusion Eng. Des. **43**, 301 (1999).

[27] D. A. Barry, S. J. Barry, and P. J. Culligan-Hensley, ACM Trans. Math. Software **21**, 172 (1995).

[28] R. M. Corless, G. H. Gonnet, D. E. G. Hare, D. J. Jeffrey, and D. E. Knuth, Adv. Comput. Math. **5**, 329 (1996).

[29] J. Boedo, A. G. McLean, D. L. Rudakov, and J. G. Watkins, Plasma Phys. Controlled Fusion **60**, 044008 (2018).

[30] R. D. Monk, A. Loarte, A. Chankin, S. Clement, S. J. Davies, J. K. Ehrenberg, H. Y. Guo, J. Lingertat, G. F. Matthews, M. F. Stamp, and P. C. Stangeby, J. Nucl. Mater. **241**, 396 (1997).

[31] R. Pitts, B. Duval, A. Loarte, J.-M. Moret, J. Boedo, D. Coster, I. Furno, J. Horacek, A. Kukushkin, D. Reiter, and J. Rommers, in *14th International Conference on Plasma-Surface Interactions in Controlled Fusion Devices* [J. Nucl. Mater. **290**, 940 (2001)].

[32]J. Horacek, R. Pitts, P. Stangeby, O. Batishchev, and A. Loarte, in *International Conference on Plasma-Surface Interactions in Controlled Fusion Devices 15* [J. Nucl. Mater. **313**, 931 (2003)].
[33]G. Fussmann, U. Ditte, W. Eckstein, T. Grave, M. Keilhacker, K. McCormick, H. Murmann, H. Röhr, M. Elshaer, K.-H. Steuer, Z. Szymanski, F. Wagner, G. Becker, K. Bernhardi, A. Eberhagen, O. Gehre, J. Gernhardt, G. Gierke, E. Glock, O. Gruber, G. Haas, M. Hesse, G. Janeschitz, F. Karger, S. Kissel, O. Klüber, M. Kornherr, G. Lisitano, H. Mayer, D. Meisel, E. Müller, W. Poschenrieder, F. Ryter, H. Rapp, F. Schneider, G. Siller, P. Smeulders, F. Söldner, E. Speth, A. Stäbler, and O. Vollmer, J. Nucl. Mater. **128**, 350 (1984).
[34]J. Watkins, O. Batishchev, J. Boedo, D. Hill, C. Lasnier, R. Lehmer, A. Leonard, and R. Moyer, J. Nucl. Mater. **266**, 980 (1999).
[35]G. McCracken, M. Stamp, R. Monk, A. Meigs, J. Lingertat, R. Prentice, A. Starling, R. Smith, and A. Tabasso, Nucl. Fusion **38**, 619 (1998).
[36]D. Lumma, J. L. Terry, and B. Lipschultz, Phys. Plasmas **4**, 2555 (1997).
[37]B. Lipschultz, J. Terry, C. Boswell, S. Krasheninnikov, B. LaBombard, and D. Pappas, J. Nucl. Mater. **266-269**, 370 (1999).
[38]J. A. Boedo, G. D. Porter, M. J. Schaffer, R. Lehmer, R. A. Moyer, J. G. Watkins, T. E. Evans, C. J. Lasnier, A. W. Leonard, and S. L. Allen, Phys. Plasmas **5**, 4305 (1998).
[39]N. Ohno, N. Tanaka, N. Ezumi, D. Nishijima, and S. Takamura, Contrib. Plasma Phys. **41**, 473 (2001).
[40]P. C. Stangeby, Plasma Phys. Controlled Fusion **37**, 1031 (1995).
[41]O. V. Batishchev, X. Q. Xu, J. A. Byers, R. H. Cohen, S. I. Krasheninnikov, T. D. Rognlien, and D. J. Sigmar, Phys. Plasmas **3**, 3386 (1996).
[42]M. Jaworski, M. Bell, T. Gray, R. Kaita, I. Kaganovich, J. Kallman, H. Kugel, B. LeBlanc, A. McLean, S. Sabbagh, F. Scotti, V. Soukhanovskii, and D. Stotler, in *Proceedings of the 20th International Conference on Plasma-Surface Interactions in Controlled Fusion Devices* [J. Nucl. Mater. **438**, S384 (2013)].
[43]K. Verhaegh, B. Lipschultz, B. Duval, J. Harrison, H. Reimerdes, C. Theiler, B. Labit, R. Maurizio, C. Marini, F. Nespoli, U. Sheikh, C. Tsui, N. Vianello, and W. Vijvers, in *Proceedings of the 22nd International Conference on Plasma Surface Interactions 2016, 22nd PSI* [Nucl. Mater. Energy **12**, 1112 (2017)].
[44]D. Brunner, B. LaBombard, R. M. Churchill, J. Hughes, B. Lipschultz, R. Ochoukov, T. D. Rognlien, C. Theiler, J. Walk, M. V. Umansky, and D. Whyte, Plasma Phys. Controlled Fusion **55**, 095010 (2013).
[45]J. Adamek, J. Horacek, J. Seidl, H. W. Müller, R. Schrittwieser, F. Mehlmann, P. Vondracek, S. Ptak, COMPASS Team, and ASDEX Upgrade Team, Contrib. Plasma Phys. **54**, 279 (2014).
[46]S. Tierno, E. Roibás, J. Doménech-Garret, J. Donoso, and L. Condo, Contrib. Plasma Phys. **53**, 16 (2013).
[47]B. Nold, T. T. Ribeiro, M. Ramisch, Z. Huang, H. W. Müller, B. D. Scott, U. Stroth, and ASDEX Upgrade Team, New J. Phys. **14**, 063022 (2012).
[48]P. C. Stangeby, J. Phys. D: Appl. Phys. **15**, 1007 (1982).
[49]K. Guenther, A. Herrmann, M. Laux, P. Pech, and H.-D. Reiner, J. Nucl. Mater. **176**, 236 (1990).
[50]D. Tskhakaya, S. Jachmich, T. Eich, and W. Fundamenski, in *Proceedings of the 19th International Conference on Plasma-Surface Interactions in Controlled Fusion* [J. Nucl. Mater. **415**, S860 (2011)].
[51]T. K. Popov, P. Ivanova, J. Stöckel, and R. Dejarnac, Plasma Phys. Controlled Fusion **51**, 065014 (2009).
[52]M. Jaworski, M. Bell, T. Gray, R. Kaita, J. Kallman, H. Kugel, B. LeBlanc, A. McLean, S. Sabbagh, V. Soukhanovskii, D. Stotler, and V. Surla, in *The 2nd International Symposium of Lithium Application for Fusion Devices* [Fusion Eng. Des. **87**, 1711 (2012)].
[53]P. C. Stangeby, J. Nucl. Mater. **128**, 969 (1984).
[54]J. W. Hughes, A. E. Hubbard, D. A. Mossessian, B. LaBombard, T. M. Biewer, R. S. Granetz, M. Greenwald, I. H. Hutchinson, J. H. Irby, Y. Lin, E. S. Marmar, M. Porkolab, J. E. Rice, J. A. Snipes, J. L. Terry, S. Wolfe, and K. Zhurovich, Fusion Sci. Technol. **51**, 317 (2007).